Characterization of anisole sooting properties in a laminar coflow diffusion lame

C Barrera, V Castro, F Escudero, J J Cruz, I Verdugo, J Yon, A Fuentes

CHARACTERIZATION OF ANISOLE SOOTING PROPERTIES IN A LAMINAR COFLOW DIFFUSION FLAME

C. Barrera[1], V. Castro[1], F. Escudero[1], J.J. Cruz[1], I. Verdugo[1], J. Yon[2], A.Fuentes[1,*]

andres.fuentes@usm.cl

[1]Departamento de Industrias, Universidad Técnica Federico Santa María, Av. España 1680, Valparaíso, Chile

[2]Normandie Univ, UNIROUEN, INSA Rouen, CNRS, CORIA, 76000

Abstract

Accumulation of greenhouse gaseous and particulate matter on the atmosphere has resulted on the search for clean energy sources to replace conventional hydrocarbon fuels. Lately, oxygenated fuels such as anisole have gained increased attention, since their addition to gasoline increases its octane number and improves the engine performance. As there are limited studies concerning soot production of anisole under enriched oxidizing environments, this study focuses on the detailed characterization of soot propensity and maturity of a well-controlled laminar coflow diffusion flame fueled with anisole and using methane as the carrier gas. Four flames established in flow conditions below the smoke point are studied. The oxidizer composition ranged from a molar fraction of oxygen on the oxidizer (oxygen index, OI) of 21% (ambient air) to 35% (doped with pure oxygen), while keeping constant the total volumetric flow rate of oxidizer. Multi-wavelength line-of-sight attenuation experiments were performed from visible to infrared wavelengths, and the measurements of the extinction coefficient and flame temperature were used to retrieve two dimensional fields of soot temperature, volume fraction, radiative intensity and degree of maturity. In general, the sooting propensity and radiative behavior of the anisole flames follows a similar tendency than typical hydrocarbon fuels when increasing the OI. However, soot volume fraction is more concentrated at the flame centerline, specially for ambient air conditions of the oxidizer. As the OI increases, temperature increases, promoting formation and oxidation processes, specially at the locations near the maximum soot volume fraction. In general, the maturity of soot particles increases as the OI increases (more graphitic particles), and from the centerline to the flame wings, for the different conditions studied. A statistical analysis of the different fields showed that, overall, the soot particles produced in the anisole flame are more mature for higher temperature environments at increased OI conditions. These results constitute a rich database for validating detailed soot production models of complex fuels, and to gain further insights on soot production of these fuels under different oxidizing environments.

Introduction

Nowadays, combustion processes of conventional fuels have become a major environmental concern due to the emission of greenhouse gases and particulate matter generated on high temperature processes, which not only contribute to global warming but also put the health of the human population at risk [1]. In an attempt to reduce these emissions, oxygenated fuels such as alcohols, ethers, and non-edible oils have been suggested to be used as blends with biodiesel [2]. It is expected that as the presence of oxygenated fuels is increased, the combustion efficiency will improve and emissions will be reduced [3]. Thus, these alternative fuels have been proposed as partial or total replacement of conventional fuels currently used. Among oxygenated alternative fuels, one that has gained increased attention is anisole (C_7H_8O). Anisole is an oxygenated aromatic fuel which is obtained from lignin processing. It has the potential to be

used as biofuel in diesel engines through its blending with conventional fuels like n-heptane [4], which is known by its low toxicity, tendency to suppress soot formation, and contribution to reduce hydrocarbon (HC) and CO emissions [5]. However, there are limited studies that deal with soot formation characteristics in anisole flames. For example, Zhang et. al [6] studied the effects of anisole and toluene addition to n-heptane. Through combination of experimental measurements and a kinetic model, they found that toluene and anisole addition resulted in notable differences on the PAH growth processes. Wang et. al [7] studied the characteristics of soot formation on anisole and benzyl alcohol blends with n-heptane at atmospheric and elevated pressure, observing an enhancement on soot formation processes with increasing oxygenated additives. In addition, they found a power-law increasing dependence of soot volume fraction with pressure, which was larger with the addition of anisole than pure n-heptane.

Besides paying attention to the fuel used, it is also important to take into account the oxidizing environment in which the fuel is burned. The more oxygen on the coflow oxidizer, the less nitrogen is available, reducing the energy losses by sensible heat. In addition, increased oxygen will result in higher flame temperatures, enhancing soot formation processes, but also enhancing oxidation processes both for availability of oxygen and increased temperature. Several studies have analyzed the effect of the oxygen molar fraction on the coflow oxidizer (oxygen index, OI) of a diffusion flame in terms of soot production, temperature, and thermal radiation from the flame [8–10]. However, only limited studies have focused on the effect of the oxygen index on sooting propensity of anisole [4].

In this study, we focus on characterizing experimentally the sooting propensity and maturity of an anisole laminar coflow diffusion flame, under different oxygen-enriched environments. Specifically, the flame characterization is based on non-intrusive optical diagnostics of multi-wavelength line-of-sight attenuation measurements, allowing to compute soot volume fraction (f_s), temperature (T_s), local radiative power per unit volume ($\nabla \cdot \dot{q}_R$), and a degree of maturity of soot particles (through a maturity coefficient β). The purpose of this study is twofold. First, to use the retrieved flame properties under different oxygen indices to better understand the soot formation and oxidation processes of anisole, and second, to construct a comprehensive database of two-dimensional fields of these properties for validation of detailed soot production models for complex liquid fuels, such as anisole.

Experimental methodology

Experimental apparatus and procedures

Figure 1 shows a schematic of the experimental setup used for the multiwavelength line-of-sight attenuation (MW-LOSA) measurements. A modified version of the Gülder burner (6) [11] was used to produce the laminar coflow diffusion flames. To avoid fuel condensation, the fuel tube and outer surface are heated with silicon heater bands and insulated by a Ertalon black cover. The temperature of the heater was controlled by a temperature controller Omega CN7533 1/32 (5). To generate a stable coflow laminar flame, anisole is mixed with a carrier gas, and injected into the inner tube of the burner. The carrier gas is methane, which is expected to not greatly affect soot formation processes of the anisole fuel [12]. The liquid anisole was stored (1) and pressurized (2) using N_2, and then delivered to a vapour delivery module (VDM, Bronkhorst SW-100 (3)) at a pressure of 3 bar. The VDM is used to vaporize the fuel at 175ºC, and a Coriolis mass flow controller (Bronkhorst F-201CV-500 (9)) is used to precisely control the fuel mass flow. The vaporized fuel was delivered to the burner through a 175ºC heated hose (4). Based on a previous study [11], the volumetric flow rate of methane is set at 257.5 ml/min, whereas the mass flow rate of anisole is set to 0.25 g/h, resulting on a constant molar fraction of anisole of $X_{vap} = 4.7 \times 10^{-2}$. These conditions result on a laminar flame with a height slightly below

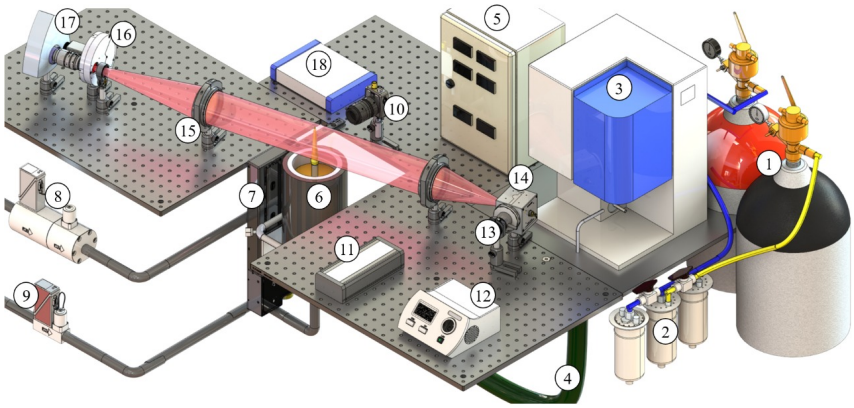

Figure 1: Experimental setup used for multi-wavelength line-of-sight attenuation measurements in the anisole flame.

Table 1: Experimental conditions for the oxidizer flow

OI (%)	21	25	31	35
Q_{air} (slpm)	140	132.91	122.28	115.19
Q_{O_2} (slpm)	0	7.09	17.72	24.81

the smoke point (SP) for all conditions. An oxidizer coflow composed of OI% of oxygen and $(1-\text{OI})$% of nitrogen was injected into the coannular section of the burner, flowing at a constant volumetric flow rate of 140 slpm and controlled by MFC Brooks SLA5800 mass flow controller (8). Variations on the OI were accomplished by controlling the ambient air flow (assumed to be composed of 21% oxygen and 79% nitrogen) and doping it with pure oxygen, according to Table 1. A fast photodiode (10) coupled to a DAQ (11) was focused on the flame tip to check the flame stability through a fast Fourier transform (FFT) analysis.

Briefly, MW-LOSA consists on measuring the line-of-sight integrated flame transmissivity (τ_λ) and radiative intensity (P_λ) at different wavelengths and then, through deconvolution processes and data treatment, retrieve the local soot properties of interest. To accomplish these measurements, a modulated back-light source (12) was used to generate the projected images, following the procedure described by Yon et al. [13]. A LED source (13) coupled to an integrating sphere (14) is used to establish a diffusive light source, which is collimated by an achromatic lens of 70 mm diameter and focal length f = 150 mm (15). This beam, after traversing the flame, passes through another achromatic lens f = 400 mm which focuses the transmitted light on the sensor of an EMCCD camera (17) coupled to a filter wheel (16). Flame images with and without back-light (from the LED) were captured at each wavelength, setting the camera acquisition rate at twice the frequency of the back-light (18). During the procedure, 250 images were acquired by the EMCCD camera for the different OI conditions, with 4 different narrow-band detection wavelengths (λ = 500, 532, 660 and 810±5 nm), using different exposure times for each wavelength (0.125, 0.07, 0.013 and 0.013 s, respectively) in order to enhance signal-to-noise ratio. Finally, the EMCCD was calibrated by absolute radiance using a broadband NIST radiometric source (Labsphere USLR-V) The EMCCD camera response was recorded for each filter used, obtaining calibration factors ($\gamma = 15.5\times10^3,\ 31.2\times10^3,\ 14.6\times10^3,\ 35.5\times10^3$ W/m^3/sr) from visible to infrared, respectively.

Soot temperature

The soot temperature T_s distribution was estimated using the τ_λ and P_λ measurements from the MW-LOSA campaign. The wavelength $\lambda = 810$ nm was selected to reduce the scattering effects, which may not be negligible for wavelengths lower than 800 nm [13]. To retrieve T_s, we need information about the local absorption coefficient ($k_{a,\lambda}$) and flame emission $J_\lambda = I_\lambda^{bb} k_{a,\lambda}$, where I_λ^{bb} is the black-body intensity. An onion-peeling deconvolution process with Tikhonov regularization was used to retrieve $k_{a,\lambda}$ and J_λ at each height (z) and radial position (r) of the flame. With these properties and using Planck's law, soot temperature can be determined as:

$$T_s = \left[-\frac{k_b \lambda}{hc} \ln \left(\frac{\lambda^5 J_\lambda}{2hc^2 \gamma k_{a,\lambda}} \right) \right]^{-1} \tag{1}$$

where k_b is the Boltzmann constant, h the Planck constant, c the speed of light in vacuum, and $\gamma = 35.5 \times 10^3$ W/m^3/sr is the calibration constant determined as described previously. Details of the procedure can be found elsewhere [13].

Soot maturity

Soot maturity determination is based on the different spectral dependence of the absorption function $E(m)$ (m is the wavelength-dependent refractive index), according to the presence of organic and graphitic components on a soot particle [13, 14]. From the J_λ and T_s fields, the experimental ratios of $E(m, \lambda_i)$ were obtained at each pair of detection wavelengths (λ_i, λ_j):

$$\frac{E(m, \lambda_i)}{E(m, \lambda_j)} = \frac{J_{\lambda_i} \lambda_i I_{\lambda_j}^{bb}(T_s)}{J_{\lambda_j} \lambda_j I_{\lambda_i}^{bb}(T_s)}. \tag{2}$$

The spectral dependence of the ratio of $E(m)$ can be expressed as a power-law function of the ratio of wavelengths, controlled by an exponent β, termed maturity coefficient [13]:

$$\frac{E(m, \lambda)}{E(m, \lambda_{ref})} = \left(\frac{\lambda_{ref}}{\lambda} \right)^\beta, \tag{3}$$

where λ_{ref} is a reference wavelength and $E(m, \lambda_{ref})$ the corresponding value for the absorption function. Note that $\beta = \chi - 1$, where χ is the Ångström absorption exponent. β can be obtained as the best fit parameter which minimizes deviations of the experimental ratios of Eq. (2) and the theoretical ones from Eq. (3). From the relation described by the theoretical ratio (3), $\beta = 0$ means a non-spectral dependency (mature soot) whereas $\beta > 0$ indicates the presence of certain amount of organic compounds on the soot particle. Through the mixing law employed by Bescond et al. [14], a relationship between $E(m, \lambda)$, β and the amount of organic compounds of soot can be obtained, considering absence of amorphous soot, i.e., only organic and graphitic soot. Finally, $E(m, \lambda)$ can be obtained from this relationship and Eq. (3).

Soot volume fraction

Assuming that soot particles follow the Rayleigh-Debye-Gans approximation and the absorption cross section is proportional to their volume, the soot volume fraction (f_s) can be obtained as $f_s = \lambda k_{a,\lambda} / 6\pi E(m, \lambda)$. Soot volume fraction was obtained from the measurements of $k_{a,\lambda}$ and considering the spatial distribution of soot absorption function $E(m, \lambda)$ determined at $\lambda = 810$ nm, as detailed by Yon et al. [13].

Soot radiation

Using the experimental fields of f_s and T_s, we can solve the radiative transfer equation (RTE) in cylindrical coordinates to estimate the local flame radiation ($\nabla \cdot \dot{q}_r$), and total radiation emitted ($\dot{Q}_R$) by soot particles within the flame, as it is performed in numerical codes [15]. To solve the RTE, the discrete ordinates method (DOM) is used to discretize the whole solid angle (ω), using a T_3 quadrature [16, 17]. The solution of the RTE provide the directional radiative intensities I_λ. Then, $\nabla \cdot \dot{q}_r$ is computed by integrating the contributions for all wavelengths and directions as:

$$\nabla \cdot \dot{q}_R = \int_0^\infty \left(4\pi k_{a,\lambda} I_\lambda^{bb} - k_{a,\lambda} \int_{4\pi} I_\lambda d\omega \right) d\lambda \tag{4}$$

The total radiation emitted by the anisole flame is computed integrating Eq. 4 over the complete flame volume:

$$\dot{Q}_r = 2\pi \iint_0^\infty \nabla \cdot \dot{q}_r r dr dz. \tag{5}$$

Error propagation

A Montecarlo error-propagation analysis was performed to quantify the uncertainties of each soot property. The measured fields of τ_λ and P_λ were perturbed by adding a Gaussian noise of zero mean and standard deviation derived from experimental measurements using the 250 images. Then the whole procedure for retrieving each property was performed for 75 generated samples. The statistical analysis of these provide values for the mean and standard deviation of each soot property, which are the error bars provided on the subsequent plots. Further information can be found on the Supplementary Material.

Results and discussions

Fields distribution

Figure 2 shows the experimentally retrieved fields for soot temperature, volume fraction, radiation and maturity coefficient (from top to bottom) for increasing oxygen enrichment conditions (from left to right). The overall features of the flame when increasing the oxygen content are similar to those encountered on typical hydrocarbons [8]. Figure 2(a) shows the temperature fields computed using Eq. 1. Overall, the flame temperature increases as the OI is increased, specially near the flame edges. The mean temperature is reported on the top of each field, showing monotonic increase from 1638 K to 1830 K as the OI is incremented from 21% to 35%.

The increase on the soot temperature results on an increase of soot volume fraction, as shown on Fig. 2(b). The total soot loading, defined as the volume integral of f_s, $\Gamma = 2\pi \iint_0^\infty f_s r dr dz$, is indicated at the top of each field. The f_s distribution is spread through the flame zone at OI = 21%, meaning that both the center and wing zones of the flame present similar soot loadings. As the OI is increased, f_s is higher on the whole, and f_s on the wings is promoted more than f_s on the center zone of the flame. This suggests that the hydrogen-abstraction carbon-addition (HACA) mechanism, that controls the soot loading on the flame wings, is enhanced in a more pronounced fashion as compared to the PAH condensation growth mechanism, that dominates the flame center. These effects on T_s and f_s also impact the luminous flame height. There is a monotonic decrease of the luminous flame height from approximately 53 mm for OI = 21% to 26 mm for OI = 35%. As T_s increases, soot formation processes are enhanced, resulting in higher f_s, but at the same time the oxidation processes are also enhanced due to both T_s and higher O_2 content, resulting on a shorter flame [8, 9]. It is interesting to note that, although the local soot content is increased for higher OIs, the total soot loading Γ monotonically decreases, indicating that the decrease of flame volume dominates over the increase on local f_s.

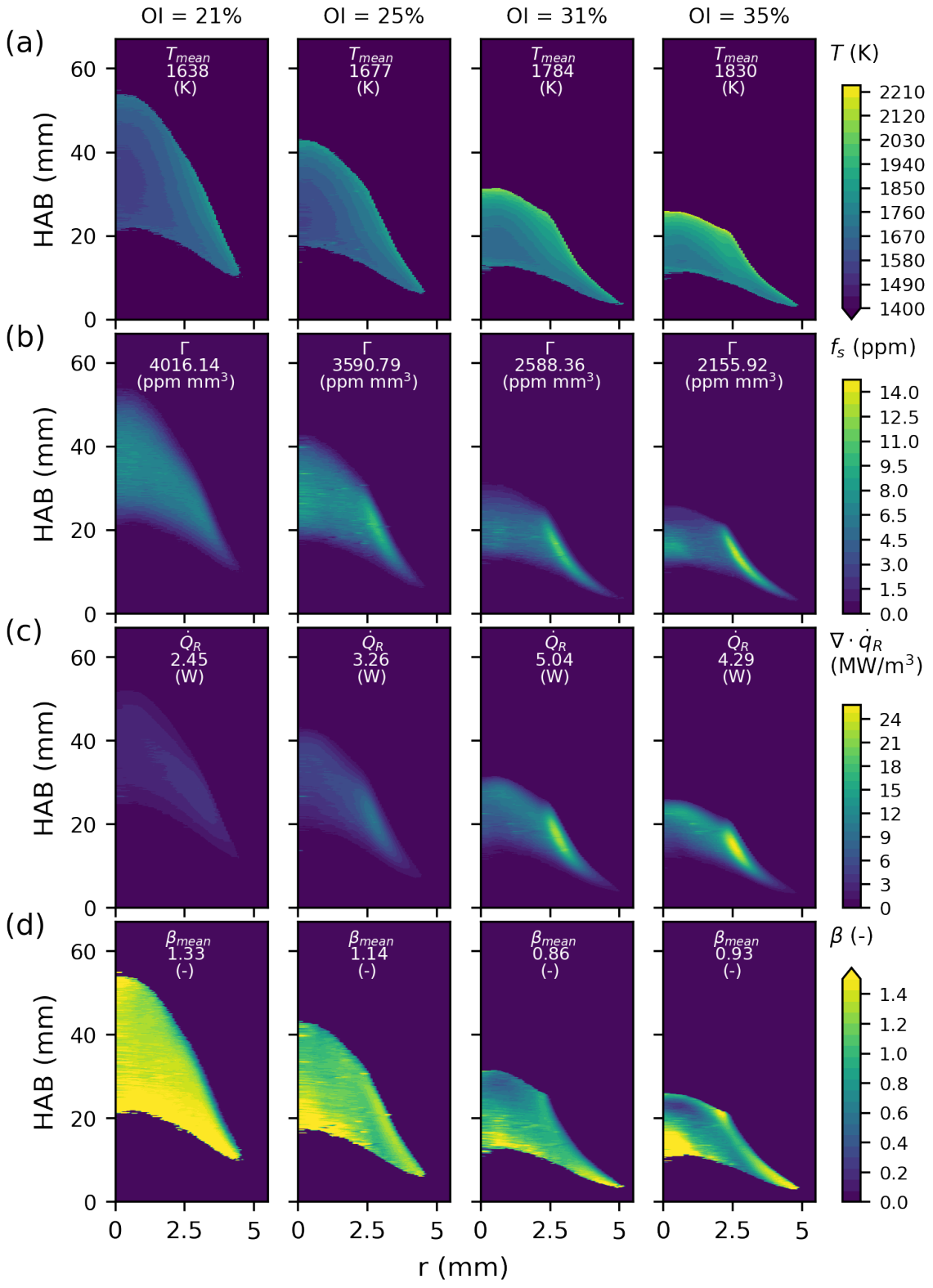

Figure 2: (a) Spatially-resolved soot volume fraction, (b) temperature, (c) divergence of the radiative heat flux computed with DOM and (d) β maturity index for different oxygen index conditions.

Fig. 2(c) presents the divergence of the radiative heat flux, which combines the effects of T_s and f_s. $\dot{Q}_R$ is indicated at the top. As the radiative calculations are performed from the infrared

(IR) to the far-infrared (FIR) region of the spectrum, the wavelength dependent absorption coefficient is assumed to be a power-law function of the ratio of wavelengths, controlled by maturity coefficient β, in the same way as for the absorption function. The reference wavelength and absorption coefficient are taken at $\lambda = 810$ nm, being the most IR measurement available. These assumptions may play a role on the absolute value of $\nabla \cdot \dot{q}_R$, but the qualitative tendencies should be well-captured. As f_s and T_s are increased, the local values of $\nabla \cdot \dot{q}_R$ are also increased as more oxygen is added to the coflow. Now it is interesting to see that the total radiation emitted by the flame (analogous to the total soot loading) presents an increase until 31%, and then starts to decrease again, indicating that the increase of total radiation due to the fourth-power of T_s and linear with f_s through the absorption coefficient, dominate over the decrease in flame volume until 31%, where these effects start to compensate.

Finally, Fig. 2(d) shows the field of maturity coefficient β. In general, for all conditions there is some spectral dependence of the ratio of absorption function ($\beta \neq 0$), indicating the presence of organic compounds within the soot particle. As the OI is increased, temperature is increased and β is decreased, evidencing that higher temperatures promoted the graphitization of soot particles. This observation is in line with the view that T_s should play a predominant role on the maturation of soot particles [18, 19].

Local analysis

In this section, a more detailed analysis of the experimental fields is developed. First, it is appropriate to define locations of interest to be analyzed. In general, centerline values of soot properties, values at the location of maximum f_s (wings), radial profiles and integrated quantities are of interest for validation of numerical models. A quantity that is useful to analyze the global amount of soot and its production rates at each height above the burner (HAB) is the radially integrated soot volume fraction, defined as $B_s = 2\pi \int_0^\infty f_s r dr$. Its derivative, dB_s/dz can be used as a measure of soot production rates, where $dB_s/dz > 0$ means that formation processes dominates over oxidation, and vice-versa. In addition, a mean formation/oxidation ($\bar{\alpha}_{for/ox}$) rate is defined as the mean value of dB_s/dz before/after $B_{s,max}$. The location of maximum B_s, or $dB_s/dz = 0$, establishes the HAB where formation and oxidation processes are balanced. This point will be taken as reference HAB for the subsequent analysis.

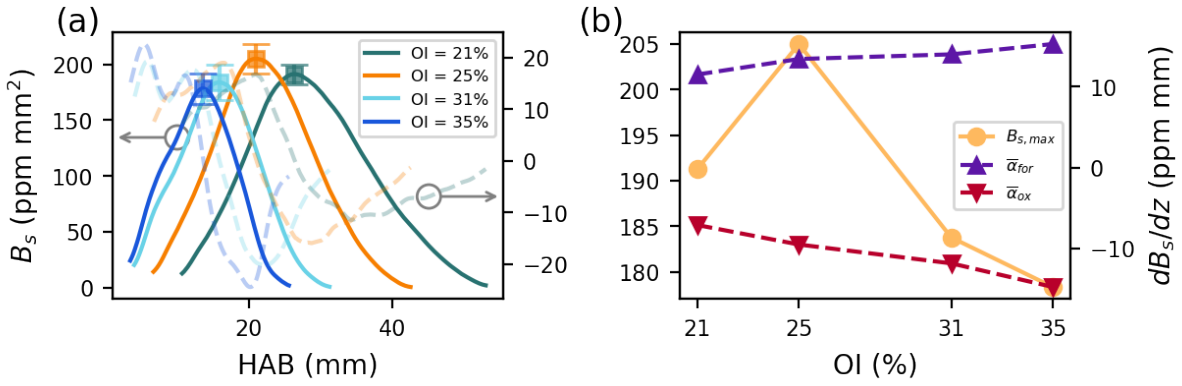

Figure 3: Radially integrated soot volume fraction B_s (continuous lines, left axis) and mean formation and oxidation rates through the slope of the B_s curve (dashed lines, right axis) as a function of the HAB.

Figure 3 shows the results for B_s for each HAB, as continuous lines at the left axis, and dB_s/dz as dashed lines at the right axis. Fig. 3(a) shows these values as a function of the

HAB, and Fig. 3(b) shows the maximum B_s and mean formation and oxidation rates. As the OI increases, the plots of B_s are shifted to lower HABs and become narrower due to the decrease in flame height. All B_s curves finish on $B_s = 0$, confirming that all flames are non-smoking. The production rates become more intense, similar to other studies [8, 20], the oxidation rates being more sensitive to the OI than the formation rates. However, the maximum values of B_s remain in a range between 177-215 ppm mm^2, indicating that the localized increase in f_s in a narrow zone near the flame wings is compensated by the decrease on flame radius.

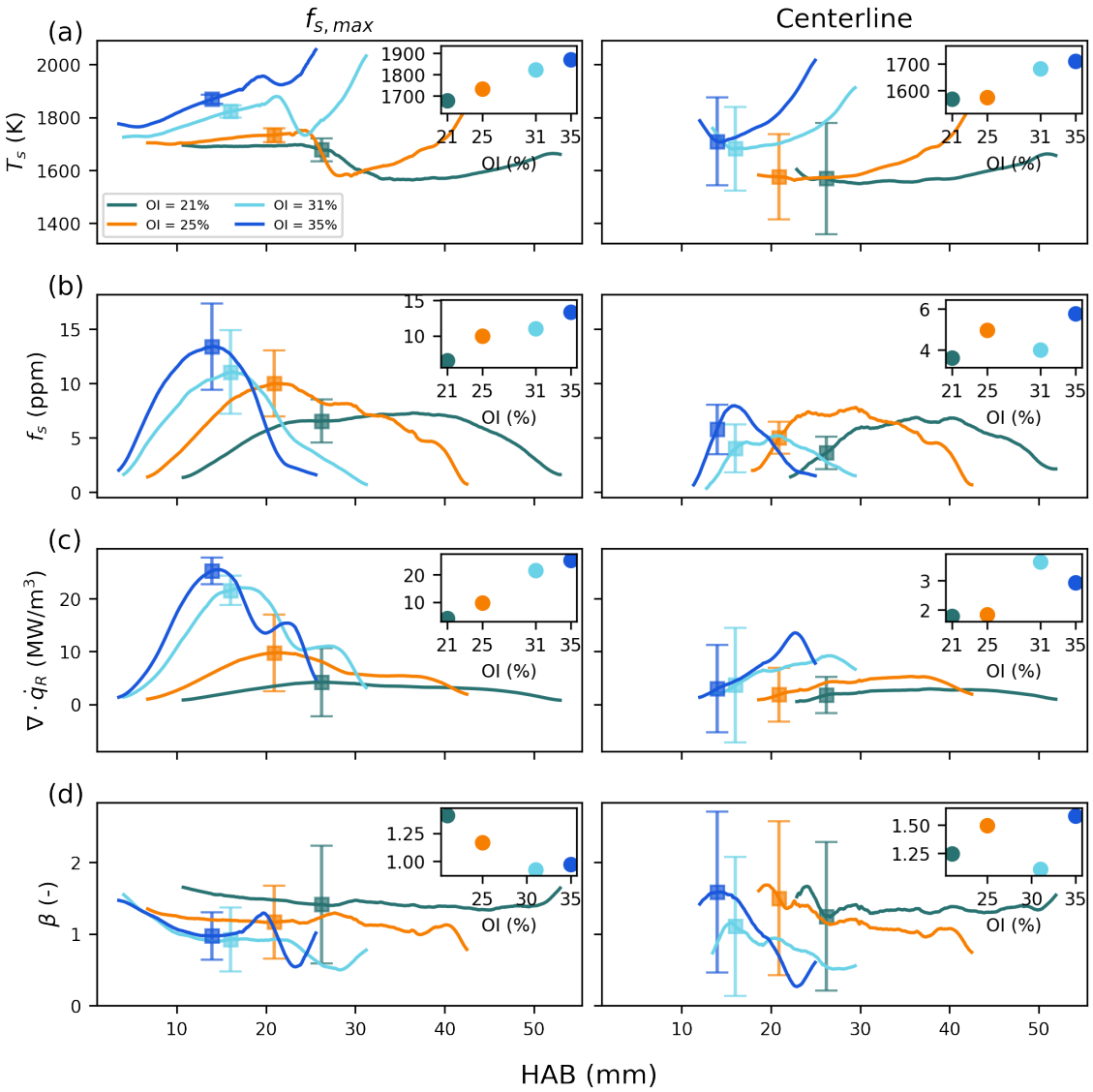

Figure 4: (a) Soot volume fraction, (b) temperature, (c) divergence of the radiative heat flux and (d) maturity coefficient at the location of the maximum f_s (left column) and the flame centerline (right column) as function of the HAB. As insets graphs, variation of each property with the OI at the HAB of maximum B_s is presented.

Fig. 4 shows the plots of the soot properties as a function of the HAB for two zones of interest, namely, the position of maximum soot volume fraction at each height (or flame wing, first column) and the flame centerline (second column). As seen on Fig. 4(a), temperature increases as the HAB is increased. There is a sharp decrease in T_s for each curve at the $f_{s,max}$ location approximately at middle of the flame for all conditions, that simply denotes the point

where the $f_{s,max}$ shifts from the wing to the flame centerline. In general, flame temperature is higher at the flame wings near the reaction zone, and at the flame tip. As the presence of oxygen in the flame increases, the maximum temperature gradually increases, reaching a peak temperature of 2234 K for an OI = 35%. Fig. 4(b) shows that f_s is promoted on the flame wings as the OI is increased, whereas f_s on the centerline remains approximately constant, between 4-6 ppm for all conditions. The HAB where B_s is maximum is almost coincident with the maximum f_s, except for an OI of 21%, where $f_{s,max}$ continues to increase until approximately an HAB of 40 mm. The increase in temperature and soot volume fraction due to the enriched OI conditions, results on an increase of $\nabla \cdot \dot{q}_R$, as shown in Fig. 4(c), specially at lower HABs on the flame wings where the production of soot is more promoted. The maximum values of $\nabla \cdot \dot{q}_r$ almost coincide with the maximum B_s, near the zone where oxidation starts to dominate over formation processes. Finally, the maturity coefficient β is lower at the location of maximum f_s than at the flame centerline, showing that more mature particles are found near the high-temperature reaction zone of the flame near the wings.

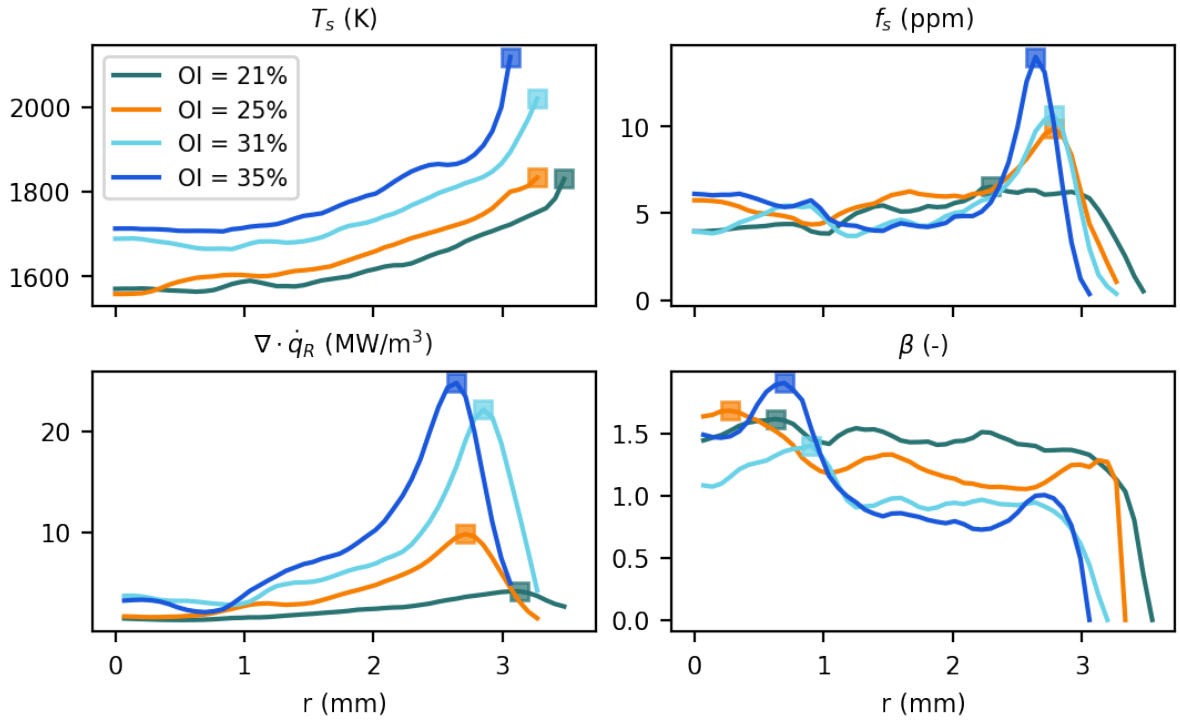

Figure 5: Radial profiles of (a) f_s, (b) T_s, (c) $\nabla \cdot \dot{q}_r$ and (d) β on the $B_{s,max}$ HAB location

Figure 5 shows the radial profiles of the flame properties at the height of maximum B_s. Temperatures increase with increasing presence of oxygen on the coflow, and from the flame center to the wing, in a similar fashion for the different OI conditions. The non-smoothness of soot volume fraction comes from the consideration of spatial variation of $E(m)$, that in turn comes from the results of β. The global features already discussed are also present on this plot, where the soot volume fraction at the wings is affected in a more pronounced way than the centerline as the OI is increased, and this behavior is repeated for $\nabla \cdot \dot{q}_R$. Finally, the maturity coefficient β follows a decreasing tendency from the center of the flame wing, the variation being more prominent as OI is increased.

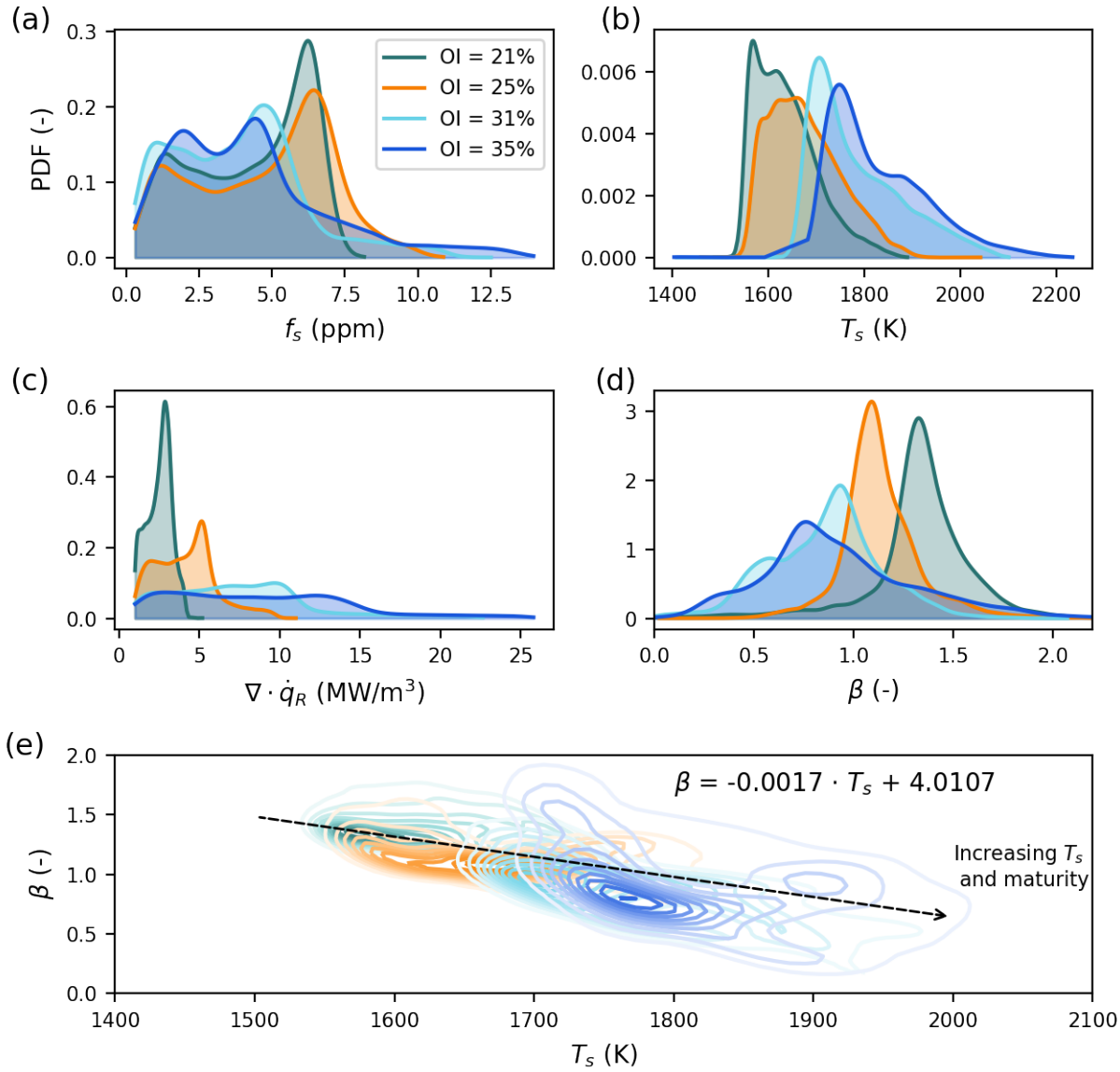

Figure 6: (a)-(d) Probability density function generated from each property of the soot over the entire flame. (e) Plot of β vs T_s for every point of the flame, with a linear fit of all the data and its equation.

Figure 6(a)-(d) shows the probability density function (PDF) of soot properties, representing the whole information of each flame. As the OI is increased, there is higher occurrence of elevated f_s, but the low value of its PDF denotes that these values are localized, as seen on the fields distributions. There is a clear shift to the right (higher temperature) for the PDFs of T_s as the OI is increased, and a similar behavior is observed for the local radiation. Finally, it is interesting to note that the PDF of the maturity coefficient seems to correlate to the T_s; higher temperatures results on lower β. Figure 6(e) shows the plot T_s with their corresponding β, for each position (r, z) within the flame. We can observe that as the temperature increases, there is an overall decrease of the maturity coefficient β, meaning that on the whole, particles are more graphitized at higher OIs. At an OI of 35%, the plot is more spread, meaning that for the same temperature, there is a wide range of maturity levels of the particles that are exposed to that temperature. This may be due to the effect of amorphous components that are not taken into consideration in this study, or the time-temperature histories of soot particles. Further studies with other fuels and coupled with numerical simulations are needed to decouple these chemical

effects, and to provide more insights about the maturation and soot production processes on complex fuels such as anisole.

Conclusions

An experimental study consisting on multi-wavelength line-of-sight attenuation measurements was performed to provide further insights of soot production and maturation processes in anisole fueled flames at different oxygen-enriched conditions. Two dimensional field distributions of soot temperature, volume fraction (taking into account the spatial variation of soot absorption function), divergence of the radiative heat flux, and maturity coefficient, were computed from flame extinction and emission measurements and analyzed in a global and local fashion. In general, as the oxygen index (OI) is increased, soot formation and oxidation processes are enhanced, resulting on higher local soot loadings, and flames that are shorter and more luminous. These results are inline with observations on typical hydrocarbons at different OIs. In addition, the maturity coefficient β, was found to decrease on the whole as the OI is increased, which suggested that there is a correlation between high temperatures and lower β (higher amount of graphitic contents). Through the analysis of the PDFs of the different properties, and visualizing the correlation between β and temperature, it was found that higher temperatures produce more graphitic soot in the studied anisole flames. For the same temperature, there is a range of maturity levels that the particles can achieve, which may depend on the time-temperature history of the soot particle.

Acknowledgments

This work was partially funded by Chile's ANID projects FONDECYT/Regular XXXX, FONDECYT/Postdoctoral 3210498 and 3190860, new PIA/ANILLO ACTXXXX?.

References

[1] B Kumfer and I Kennedy. "The role of soot in the health effects of inhaled airborne particles". In: *Combustion generated fine carbonaceous particles (proceedings of an international workshop held in Villa Orlandi, Anacapri, May 13–16, 2007)*. KIT Scientific Publishing. 2009, pp. 1–15.

[2] Ajay Singh Verma et al. "A review on performance, combustion and emissions utilizing alternative fuels". In: *Materials Today: Proceedings* (2022).

[3] S Kalligeros et al. "An investigation of using biodiesel/marine diesel blends on the performance of a stationary diesel engine". In: *Biomass and Bioenergy* 24.2 (2003), pp. 141–149.

[4] Gaihua Xiong et al. "Sooting tendency of n-heptane/anisole blends in laminar counterflow flames with oxygen enrichment". In: *Fuel* 255 (2019), p. 115820.

[5] A. Rajesh et al. "Effect of anisole addition to waste cooking oil methyl ester on combustion, emission and performance characteristics of a DI diesel engine without any modifications". In: *Fuel* 278 (2020), p. 118315.

[6] Yiran Zhang et al. "Chemical effects of anisole and toluene addition to n-heptane on PAH characteristics in laminar premixed flames by LIF measurement and kinetic model". In: *Fuel* 303 (2021), p. 121255.

[7] Wenyu Wang et al. "Study of soot formations in co-flow laminar diffusion flames of n-heptane and oxygenated aromatic biofuels from atmospheric condition to 2.3 bar". In: *Fuel* 297 (2021), p. 120753.

[8] F. Escudero et al. “Unified behavior of soot production and radiative heat transfer in ethylene, propane and butane axisymmetric laminar diffusion flames at different oxygen indices”. In: *Fuel* 183 (2016), pp. 668–679.

[9] Daniela Cortés et al. “Effect of Fuels and Oxygen Indices on the Morphology of Soot Generated in Laminar Coflow Diffusion Flames”. In: *Energy & Fuels* 32 (Oct. 2018).

[10] Francisco Cepeda et al. “Influence of the oxygen index on acoustically forced laminar ethylene non-premixed flames”. In: *Combustion and Flame* 236 (2022), p. 111745.

[11] F. Patiño et al. “Soot primary particle sizing in a n-heptane doped methane/air laminar coflow diffusion flame by planar two-color TiRe-LII and TEM image analysis”. In: *Fuel* 266 (2020), p. 117030.

[12] Yuhan Zhu et al. “Experimental study on the effect of hydrogen addition on methane/ethylene diffusion flame soot formation based on light extinction measurement”. In: *Energy Reports* 7 (2021). 2021 International Conference on Energy Engineering and Power Systems, pp. 673–683.

[13] Jérôme Yon et al. “Revealing soot maturity based on multi-wavelength absorption/emission measurements in laminar axisymmetric coflow ethylene diffusion flames”. In: *Combustion and Flame* 227 (2021), pp. 147–161.

[14] A. Bescond et al. “Soot optical properties determined by analyzing extinction spectra in the visible near-UV: Toward an optical speciation according to constituents and structure”. In: *Journal of Aerosol Science* 101 (2016), pp. 118–132.

[15] Nick A Eaves et al. “CoFlame: A refined and validated numerical algorithm for modeling sooting laminar coflow diffusion flames”. In: *Computer Physics Communications* 207 (2016), pp. 464–477.

[16] C. P. Thurgood, A. Pollard, and H. A. Becker. “The TN Quadrature Set for the Discrete Ordinates Method”. In: *Journal of Heat Transfer* 117.4 (Nov. 1995), pp. 1068–1070. eprint: `https://asmedigitalcollection.asme.org/heattransfer/article-pdf/117/4/1068/5910900/1068\_1.pdf`.

[17] “Non-grey gas radiative transfer analyses using the statistical narrow-band model”. In: *International Journal of Heat and Mass Transfer* 41.14 (1998), pp. 2227–2236.

[18] Mohammad Reza Kholghy, Armin Veshkini, and Murray John Thomson. “The core–shell internal nanostructure of soot–A criterion to model soot maturity”. In: *Carbon* 100 (2016), pp. 508–536.

[19] Hope A Michelsen et al. “A review of terminology used to describe soot formation and evolution under combustion and pyrolytic conditions”. In: *ACS nano* 14.10 (2020), pp. 12470–12490.

[20] Francisco Cepeda et al. “Impact of water-vapor addition to oxidizer on the thermal radiation characteristics of non-premixed laminar coflow ethylene flames under oxygen-deficient conditions”. In: *Fire Safety Journal* 120 (2021). Fire Safety Science: Proceedings of the 13th International Symposium, p. 103032.

Supplementary material

Soot absorption function

Figure S1 shows the fields of absorption function obtained at 810 nm.

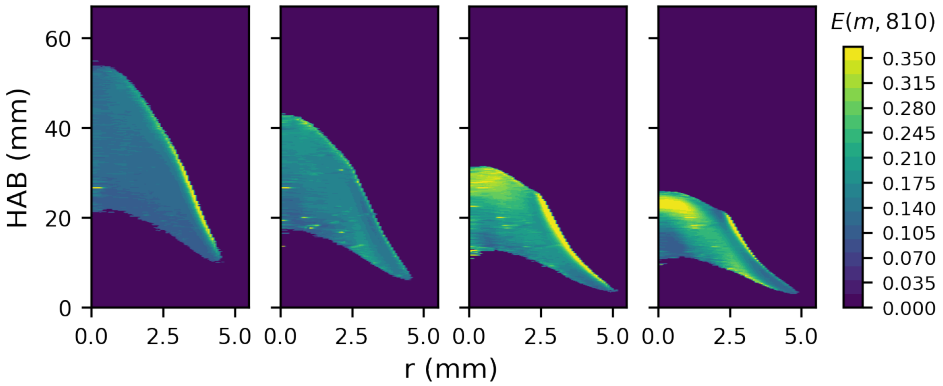

Figure S1: Absorption function of soot at different oxygen indices for a wavelength $\lambda = 810$ nm.

Uncertainty analysis

The fields of relative errors for T_s, f_s, $\nabla \cdot \dot{q}_R$, β, and $E(m, 810)$, defined as the values of the standard deviation (denoted as δ) divided by the mean value (denoted by an overbar), is shown in Fig. S2. These error were computed using 75 perturbed fields using the mean and standard deviation from the experimental measurements of τ_λ and P_λ.

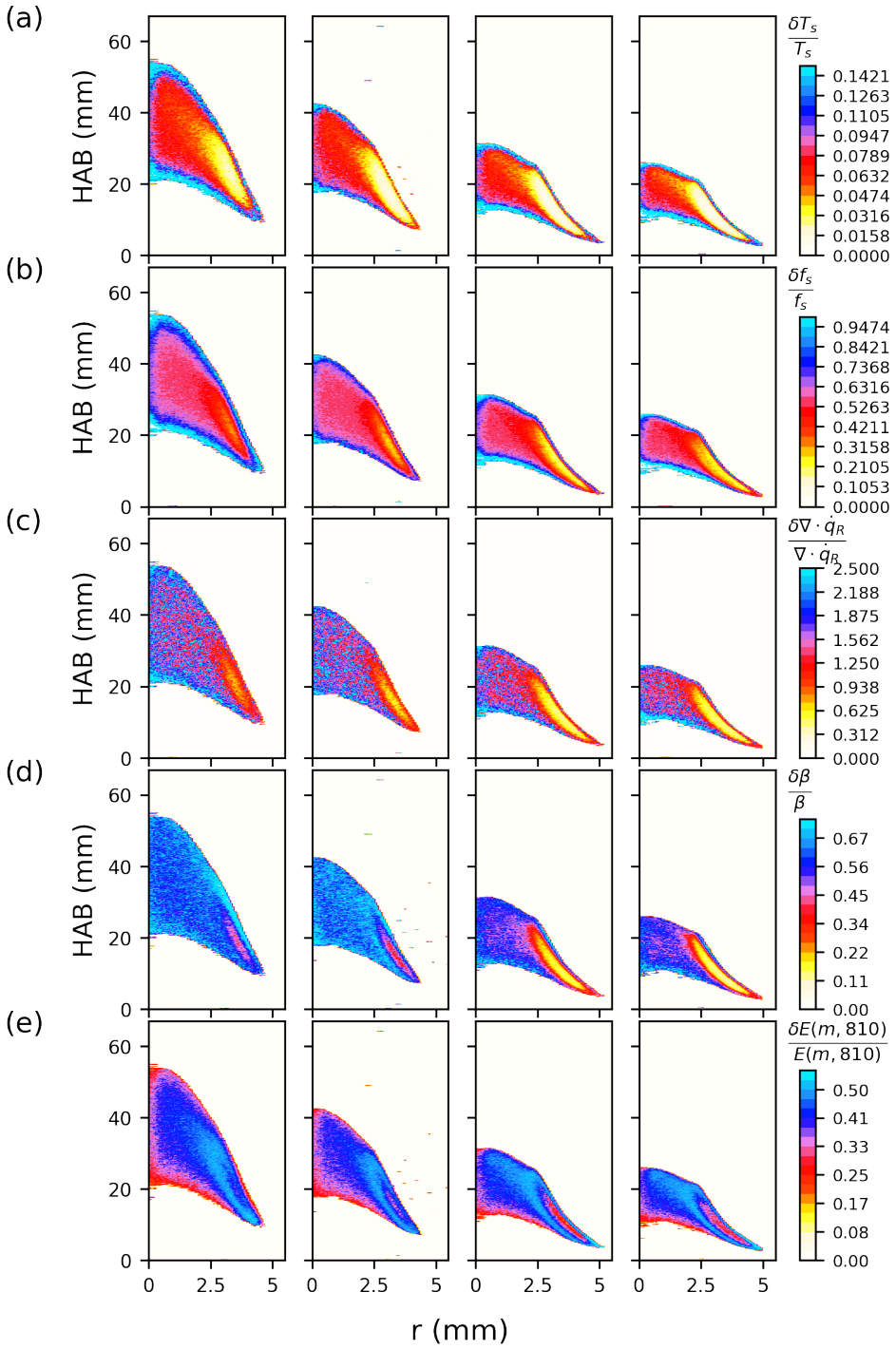

Figure S2: Relative errors for (a) soot volume fraction, (b) temperature, (c) divergence of the radiative heat flux, (d) β maturity index and (e) absorption function at 810 nm, for different oxygen index conditions.